Band inversion driven by electronic correlations at the (111) LaAlO₃/SrTiO₃ interface

A. M. R. V. L. Monteiro,[1,*] M. Vivek,[2] D. J. Groenendijk,[1] P. Bruneel,[2] I. Leermakers,[3] U. Zeitler,[3]
M. Gabay,[2] and A. D. Caviglia[1]

[1]*Kavli Institute of Nanoscience, Delft University of Technology, P.O. Box 5046, 2600 GA Delft, The Netherlands*
[2]*Laboratoire de Physique des Solides, Université Paris-Sud 11, Université Paris Saclay, CNRS UMR 8502, 91405 Orsay Cedex, France*
[3]*High Field Magnet Laboratory (HFML-EFML), Radboud University Nijmegen, 6525 ED Nijmegen, The Netherlands*

Quantum confinement at complex oxide interfaces establishes an intricate hierarchy of the strongly correlated d orbitals which is widely recognized as a source of emergent physics. The most prominent example is the (001) LaAlO₃/SrTiO₃ (LAO/STO) interface, which features a dome-shaped phase diagram of superconducting critical temperature and spin-orbit coupling (SOC) as a function of electrostatic doping, arising from a selective occupancy of t_{2g} orbitals of different character. Here we study (111)-oriented LAO/STO interfaces, where the three t_{2g} orbitals contribute equally to the subband states caused by confinement, and investigate the impact of this unique feature on electronic transport. We show that transport occurs through two sets of electronlike subbands, and the carrier density of one of the sets shows a nonmonotonic dependence on the sample conductance. Using tight-binding modeling, we demonstrate that this behavior stems from a band inversion driven by on-site Coulomb interactions. The balanced contribution of all t_{2g} orbitals to electronic transport is shown to result in strong SOC with reduced electrostatic modulation.

Complex oxide interfaces display a variety of emergent physical properties that arise from their highly correlated d electrons and are therefore absent in conventional semiconductor quantum wells [1,2]. The two-dimensional electron system (2DES) at the interface between LaAlO₃ (LAO) and (001)-oriented SrTiO₃ (STO) is the prototypical oxide quantum well [3], featuring several interesting phenomena that include 2D superconductivity [4] and Rashba spin-orbit coupling (SOC) [5,6]. The hierarchy of d orbitals with different symmetries imposed by two-dimensional confinement has been recognized as a key element in determining the properties of the system [7]. In particular, it has been proposed that the dome-shaped behavior of the superconducting critical temperature (T_c) and SOC strength with electrostatic doping is related to the selective occupancy of orbitals of different character, detected by a transition from one- to two-carrier transport [8]. On the other hand, recent works have shown that the crystallographic direction of confinement is a powerful tool enabling selective modification of this band hierarchy [9–11]. (111)-oriented LAO/STO interfaces are of particular interest, since the subband structure due to quantum confinement preserves the t_{2g} manifold symmetry along this direction [12–15]. Transport studies have shown that the system condenses into a superconducting ground state [16–18] and proposed a link between T_c and SOC [5,18]. More strikingly, field-effect measurements have brought to light an unconventional behavior of the Hall coefficient (R_H), which has been interpreted as a signature of a holelike band [18–20].

In this work, we investigate the electronic properties of (111)-oriented LAO/STO interfaces and show that (i)

transport occurs solely through electronlike subbands and (ii) a subband inversion triggered by local Coulomb interactions is key to explain the unusual behavior of R_H. Importantly, we show that this inversion occurs between two sets of t_{2g} subbands, each with a balanced contribution of d_{xy}, d_{yz}, and d_{xz} character. As a direct consequence of this unique feature, SOC is strong and displays reduced electrostatic tunability.

Initially, the study of LAO/STO interfaces was restricted to the (001) crystallographic direction, where the emergence of conduction was originally explained in terms of an interfacial polar discontinuity [3,21]. In this model, a polar discontinuity arises at the interface between LAO and (001) STO [3] as a consequence of the stacking of charged ionic LAO planes (with alternating valency of $+1e$ and $-1e$) over the neutral STO planes. As a result, the voltage grows with the thickness of the LAO film until the built-in potential becomes larger than ΔE [Fig. 1(a)]. At a critical thickness $t_c \approx 3.5$ u.c., this triggers an electronic reconstruction in which half an electron per unit cell is transferred from the surface of the LAO film to Ti $3d$ states at the interface [22,23]. More recent works have shown that the polar field triggers the spontaneous formation of surface oxygen vacancies, leading to interface conductivity [24,25].

Viewed along the (111) crystallographic direction, the cubic perovskite lattice consists of three interspersing triangular lattices of Ti atoms, as shown in Fig. 1(b) (where the labels Ti 1, 2, and 3 refer to the distance of the Ti layer with respect to the interface). If a bilayer of atoms is considered, the projection of the Ti atoms onto the same plane yields a hexagonal lattice, similar to the one found in graphene. A variety of recent works have probed this sixfold symmetry, which was corroborated by the 2D Fermi surface [13,26] and anisotropic magnetotransport measurements [27,28]. The
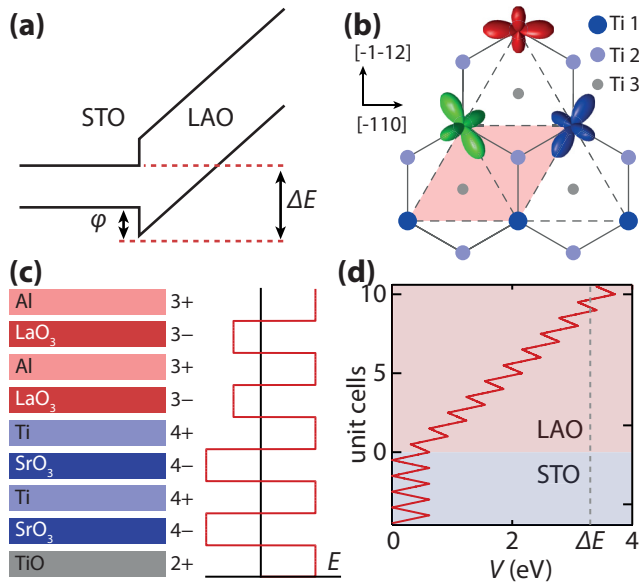
*A.M.Monteiro@tudelft.nl

FIG. 1. (a) Band diagram of the LAO/STO interface before electronic reconstruction. ΔE: critical potential buildup. ϕ: valence-band offset. (b) Top view of three consecutive (111) Ti^{4+} layers. The red shaded area represents the unit-cell cross section of a bilayer. The three t_{2g} orbitals are shown to evidence their equivalent projection onto the 2DES plane. (c) Left: stacking of ionic planes across the interface. The bottommost Ti^{4+} plane is considered to react with oxygen to form TiO^{2+}. Right: resulting electric field across the interface before the electronic reconstruction takes place. (d) Electrostatic potential as a function of the number of unit cells.

FIG. 2. (a) Carrier density (n) and mobility (μ) as a function of temperature (T) measured for the pristine state. Inset: schematic representation of the measurement configuration. (b) Superconducting critical temperature (T_c) as a function of sample conductance (σ_{tot}) for different thicknesses of the LAO film. (c) Carrier densities and (d) mobilities as a function of σ_{tot}.

(111) orientation features highly charged planes both for STO and LAO ($\pm 4e$ and $\pm 3e$, respectively). In the most simplistic ionic picture, this would bring about a diverging electrostatic potential in the STO substrate itself. To overcome this, we consider an STO(111) slab where the bottom Ti layer is oxidized [Fig. 1(c)]. In this model, the resulting potential on the STO side no longer diverges and, upon growth of the LAO layer, a polar discontinuity at the interface takes place. At the (111)-oriented interface, the interplanar distance is given by $d = a_{LAO}/\sqrt{3}$ and the unit-cell cross section A is given by the red shaded region in Fig. 1(b). Figure 1(d) shows the calculated potential buildup as a function of the number of unit cells of (111) LAO. On the STO side, the potential oscillates between a finite value and zero, and starts to diverge on the LAO side. It is worth noticing that the different formal polarization of the successive A-site and B-site sublayers gives rise to an oscillatory potential also on the LAO side, in contrast with the steplike behavior observed in the (001)-oriented case. This simple model for the intrinsic doping mechanism yields a threshold thickness $t_c = 8.5$ u.c., in good agreement with experimental studies that report a critical thickness of 9 u.c. [9]. The exact value can be slightly affected by defect states or a valence-band offset, as observed in the (001)-oriented case [29,30].

Having proposed a possible solution for the polar instability at (111)-oriented LAO/STO interfaces, we investigate the evolution of electronic properties as a function of temperature and electrostatic doping. The temperature
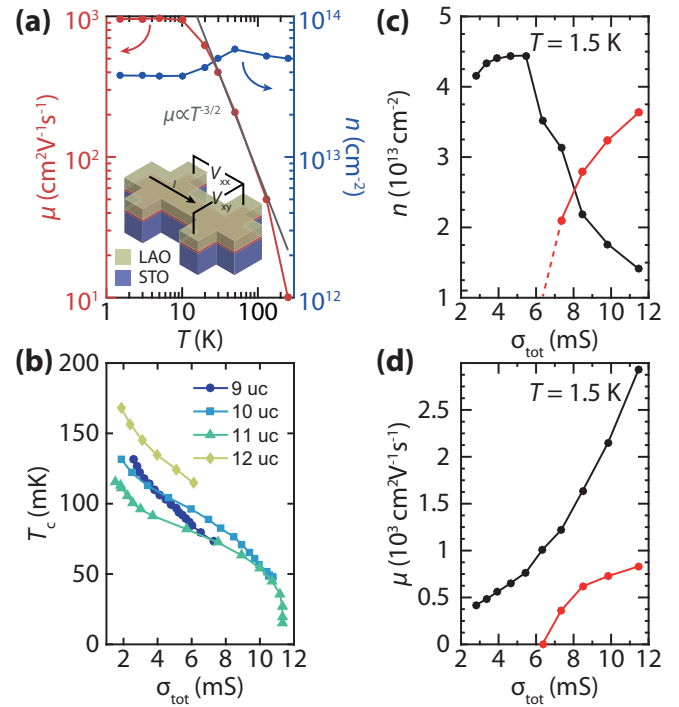
dependence of carrier density (n) and mobility (μ) for a 9-u.c. LAO/STO (111) interface is shown in Fig. 2(a). In the pristine state, the Hall effect remains linear down to 1.5 K in a range of 10 T. The extracted carrier density remains fairly constant around $(3–5) \times 10^{13}$ cm^{-2} in the entire temperature range. The mobility increases rapidly from 10 cm^2 V^{-1} s^{-1} at room temperature to a maximum value of 1000 cm^2 V^{-1} s^{-1} at 1.5 K, with saturation occurring below 10 K. The gray line represents the phonon-limited mobility $\mu_{ph} \propto T^{-3/2}$, showing good accordance with the data at high temperatures. Moreover, the carrier density values obtained are comparable with those reported for (001)-oriented interfaces.

At 1.5 K, we use a back-gate geometry to perform high-field magnetotransport measurements as a function of electrostatic doping. At high conductance values, a transition from linear to nonlinear Hall curves is observed, indicating a transition from one- to two-carrier transport. At variance with previous works [18–20], the observation of this nonlinearity enables us to unequivocally ascertain that the two bands involved in transport are electronlike, and we analytically show that the evolution of R_H as a function of B is incompatible with an electron-hole scenario (see Ref. [31] for details on the carrier types of the two bands). Figures 2(c) and 2(d) show the extracted values of carrier density ($n_{1,2}$) and mobility ($\mu_{1,2}$) by fitting the Hall curves to a two-band model (see Ref. [31] for the analysis of the Hall transport and magnetoresistance data). The appearance of the second band at

$\sigma \approx 6$ mS is readily evident: at this point, n_2 increases rapidly, seemingly at the expense of n_1. Moreover, the second band has a mobility which is roughly three times smaller than the first band. In the millikelvin regime, the system condenses into a superconducting ground state [16] and measurements of the gate-voltage-induced changes in T_c in the same conductance range reveal a monotonic decrease of T_c as the conductance is increased.

As shown in Fig. 2(b), this behavior is consistently observed in several samples, with LAO thicknesses ranging from 9 to 12 u.c.. This is in stark contrast with (001)-oriented interfaces, where the maximum of the superconducting dome occurs concomitantly with the onset of population of the $d_{xz,yz}$ bands at the Lifshitz point. In the (111) crystallographic direction, all the t_{2g} orbitals have the same geometrical projection onto the 2DES plane [see Fig. 1(b)], therefore the observed transition must have an intrinsically different origin than the one observed in the (001) counterpart.

The subband structure was determined from Poisson-Schrödinger calculations and dispersions consequently derived by means of tight-binding modeling (see Ref. [31] for details on the theoretical modeling). For the experimentally accessible range of carrier concentrations, two sets of subbands lie close to the Fermi energy E_F. These two sets of subbands, labeled 1 and 2 in Fig. 3, each contain six branches. However, due to time-reversal symmetry, there are only three different energies per set, thus leading to a six-band low-energy model. In our tight-binding calculations we include the effects of (i) confinement, (ii) bulk SOC, (iii) trigonal field, and (iv) Hubbard-type on-site interactions between like (U) and unlike (U') orbitals. Strong potential gradients and bond angle distortions at the interface lead to orbital mixing [32]. If we include this term in the Hamiltonian we find a 2–3 meV Rashba-like splitting (see Fig. S3 in Ref. [31]). However, the splitting in energy is at least one order of magnitude smaller than other energy contributions and it has no significant impact on the population inversion so it is not shown in Figs. 3(a) and 3(b). Coulomb terms cause the bands to shift by unequal amounts resulting in band crossings and in changes in the individual carrier concentrations of the bands. In order to keep the total carrier density constant before and after the inclusion of interactions, the Fermi level renormalizes. This renormalization of the Fermi level is performed in a self-consistent way (see Ref. [31] for details on the theoretical modeling). The resulting band structures are plotted in Figs. 3(a) and 3(b) where we show the energy vs momentum (E vs k) along the $k_x = 0$ direction for two different filling factors. k_y (k_x) corresponds to ΓM (ΓK) for the hexagonal Brillouin zone (BZ). Both k_x and k_y are in units of $1/c$, where $c = \sqrt{2/3}a$, and a is the Ti-Ti interatomic distance. Careful analysis of Figs. 3(a) and 3(b) readily highlights the crucial role of electron correlations in reproducing our experimental observations. At low E_F [Fig. 3(a)], only the first set of subbands is populated. At high E_F [Fig. 3(b)], the second set of subbands, which extends deeper into the substrate, becomes populated and, most importantly, a band inversion takes place. The second set of subbands becomes lower in energy, while the first subset is pushed upward. The consequences of this can be more clearly seen in the corresponding Fermi surfaces plotted in Figs. 3(c) and 3(d), where the contour of the first
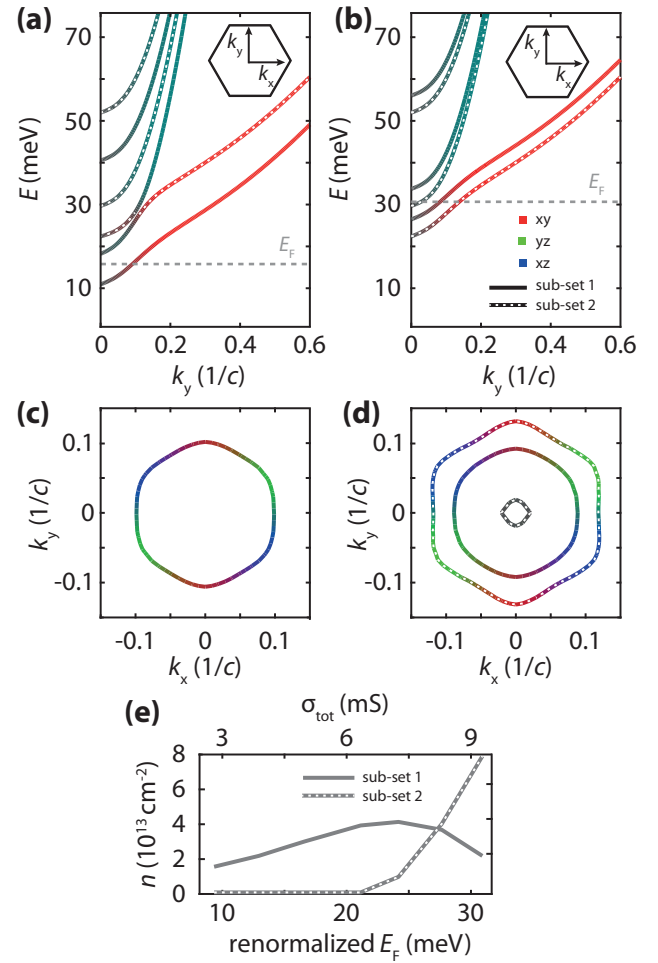

FIG. 3. (a),(b) Band structure along k_y at low and high filling, respectively. Dashed gray line indicates the renormalized Fermi level. Color indicates the orbital character. Stoke indicates the band subset. Inset shows the hexagonal Brillouin zone as well as the k_x (ΓK) and k_y (ΓM) directions. (c),(d) Corresponding Fermi surfaces. (e) Evolution of the carrier density pertaining to the first (n_1) and second (n_2) subset of bands as a function of renormalized Fermi level and respective sample conductance.

set of subbands is reduced with increasing E_F. Conversely, it is evident in Fig. 3(d) that the second subband becomes heavily populated, its contour becoming larger than that of the first subband. It is worth underscoring that, while the orbital character of each band is highly dependent on the crystallographic direction in the BZ, their overall contributions to electronic transport are nearly equal. The concentrations of the carriers in each band are summed for each subset and are shown in Fig. 3(e) as a function of E_F. The resemblance with the experimental data is striking: at low filling only the first set of subbands contributes to transport and, at a critical filling, the population of the second set of subbands starts increasing, concomitantly with a decline of the population of the first one. Our model highlights that, in contrast with the (001) case, the transition from one- to two-carrier transport in the (111) direction stems from the occupation of a second set of t_{2g} subbands as a consequence of Coulomb repulsion.
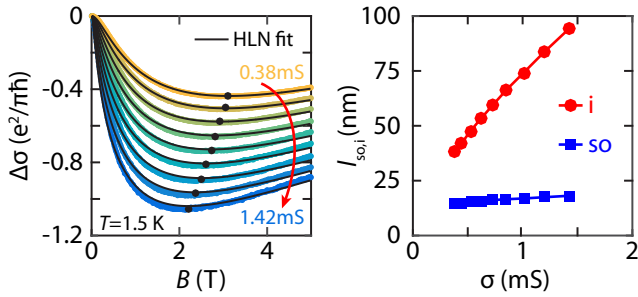
FIG. 4. (a) Variation of conductance $\Delta\sigma$ as a function of the B field for different levels of electrostatic doping. Black dots: B_{min}. Black lines: fit to the HLN equation. (b) Extracted characteristic lengths $l_{i,so}$.

If U and U' are set to zero, populations of both subsets exhibit a monotonic increase at variance with the experimental observation (see Fig. S4 in Ref. [31]).

To investigate the effects of the orbital hierarchy of (111)-oriented LAO/STO on SOC, we analyzed the field dependence of the magnetoconductance (MC) as a function of electrostatic doping. We restrict our analysis to low conductance values, where the Hall effect is linear and the classical magnetoconductance contribution is negligible [31]. As shown in Fig. 4(a), negative MC is observed in the entire range of conductance explored, in accordance with previous work [18]. For a 2D diffusive metallic system placed in a perpendicular magnetic field (B), the quantum corrections to conductance are given by the Hikami-Larkin-Nagaoka (HLN) model [33]:

$$\frac{\Delta\sigma(B)}{\sigma_0} = -\left[\frac{1}{2}\Psi\left(\frac{1}{2}+\frac{B_i}{B}\right) - \frac{1}{2}\ln\frac{B_i}{B}\right.$$
$$- \Psi\left(\frac{1}{2}+\frac{B_i+B_{SO}}{B}\right) + \ln\frac{B_i+B_{SO}}{B}$$
$$\left.- \frac{1}{2}\Psi\left(\frac{1}{2}+\frac{B_i+2B_{SO}}{B}\right) + \frac{1}{2}\ln\frac{B_i+2B_{SO}}{B}\right],$$

$$(1)$$

where $\sigma_0 = \frac{e^2}{\pi h}$, Ψ is the digamma function, and $B_{i,SO}$ are the effective fields related to the inelastic and spin-orbit relaxation lengths, respectively. Figure 4(a) shows $\Delta\sigma$ and the respective quantum correction from the HLN model (black lines). $\Delta\sigma$ displays a local minimum at a field B_{min}, which indicates the point where weak antilocalization (WAL) is overcome by

weak localization (WL). It has been demonstrated that B_{min} is proportional to the characteristic magnetic field B_{SO} [34]. Therefore, the gradual shift of B_{min} to smaller values of B as a function of electrostatic doping indicates a monotonic decrease of the SOC strength. At variance with previous work [18], no classical component was required to fit the data and the local minima of the data are well captured by the usual quantum corrections. The characteristic lengths of inelastic and spin-orbit scattering $l_{i,so}$ are related to the effective fields by $B_{i,SO} = \hbar/4el_{i,SO}^2$ and are shown as a function of applied electrostatic doping in Fig. 4(b). We find that $l_{SO} < l_i$ throughout the entire range, indicating WAL. Moreover, we observe a relatively small value of l_{SO} which exhibits a limited variation with electrostatic doping, indicating that SO interactions are strong ($\varepsilon_{SO} \approx 4.26$ meV at 0.38 mS), but overall display reduced tunability with respect to the (001)-oriented case. This can be understood by recalling that a hallmark feature of this crystallographic direction is the identical projection of all t_{2g} orbitals onto the 2DES plane. Note also that B_{SO} is extracted from HLN fits for sigma values smaller than those considered in Fig. 2.

In summary, we have studied (111)-oriented LAO/STO interfaces where t_{2g} manifold splitting by quantum confinement is absent. We demonstrate that transport occurs through electronlike subbands and on-site correlations drive an inversion between two sets of t_{2g} subbands, each containing a balanced contribution of all three orbital characters. This captures the nonmonotonic dependence of R_H on electrostatic doping and rules out the presence of a holelike band. The results of this work strongly underline the importance of orbital hierarchy and electron-electron interactions in determining the properties of two-dimensional electron systems at oxide interfaces [35].

Note added. Recently, Khanna *et al.* [35] posted a preprint probing experimentally and theoretically the role of electronic correlations at the (111)-oriented LAO/STO interface.

[1] E. Dagotto, Science **309**, 257 (2005).

[2] H. Hwang, Y. Iwasa, M. Kawasaki, B. Keimer, N. Nagaosa, and Y. Tokura, Nat. Mater. **11**, 103 (2012).

[3] A. Ohtomo and H. Hwang, Nature (London) **427**, 423 (2004).

[4] N. Reyren, S. Thiel, A. Caviglia, L. F. Kourkoutis, G. Hammerl, C. Richter, C. Schneider, T. Kopp, A.-S. Rüetschi, D. Jaccard, M. Gabay, D. Muller, J.-M. Triscone, and J. Mannhart, Science **317**, 1196 (2007).

[5] A. D. Caviglia, M. Gabay, S. Gariglio, N. Reyren, C. Cancellieri, and J.-M. Triscone, Phys. Rev. Lett. **104**, 126803 (2010).

[6] M. Ben Shalom, M. Sachs, D. Rakhmilevitch, A. Palevski, and Y. Dagan, Phys. Rev. Lett. **104**, 126802 (2010).

[7] M. Salluzzo, J. C. Cezar, N. B. Brookes, V. Bisogni, G. M. De Luca, C. Richter, S. Thiel, J. Mannhart, M. Huijben,

A. Brinkman, G. Rijnders, and G. Ghiringhelli, Phys. Rev. Lett. **102**, 166804 (2009).

[8] A. Joshua, S. Pecker, J. Ruhman, E. Altman, and S. Ilani, Nat. Commun. **3**, 1129 (2012).

[9] G. Herranz, F. Sánchez, N. Dix, M. Scigaj, and J. Fontcuberta, Sci. Rep. **2**, 758 (2012).

[10] G. Herranz, G. Singh, N. Bergeal, A. Jouan, J. Lesueur, J. Gázquez, M. Varela, M. Scigaj, N. Dix, F. Sánchez, and J. Fontcuberta, Nat. Commun. **6**, 6028 (2015).

[11] D. Pesquera, M. Scigaj, P. Gargiani, A. Barla, J. Herrero-Martín, E. Pellegrin, S. M. Valvidares, J. Gázquez, M. Varela, N. Dix, J. Fontcuberta, F. Sánchez, and G. Herranz, Phys. Rev. Lett. **113**, 156802 (2014).

[12] D. Doennig, W. E. Pickett, and R. Pentcheva, Phys. Rev. Lett. **111**, 126804 (2013).

[13] S. McKeown Walker, A. de la Torre, F. Y. Bruno, A. Tamai, T. K. Kim, M. Hoesch, M. Shi, M. S. Bahramy, P. D. C. King, and F. Baumberger, Phys. Rev. Lett. **113**, 177601 (2014).

[14] K. Song, S. Ryu, H. Lee, T. R. Paudel, C. T. Koch, B. Park, J. K. Lee, S.-Y. Choi, Y.-M. Kim, J. C. Kim *et al.*, Nat. Nanotechnol. **13**, 198 (2018).

[15] G. M. De Luca, R. Di Capua, E. Di Gennaro, A. Sambri, F. M. Granozio, G. Ghiringhelli, D. Betto, C. Piamonteze, N. B. Brookes, and M. Salluzzo, Phys. Rev. B **98**, 115143 (2018).

[16] A. M. R. V. L. Monteiro, D. J. Groenendijk, I. Groen, J. de Bruijckere, R. Gaudenzi, H. S. J. van der Zant, and A. D. Caviglia, Phys. Rev. B **96**, 020504(R) (2017).

[17] S. Davis, Z. Huang, K. Han, Ariando, T. Venkatesan, and V. Chandrasekhar, Phys. Rev. B **96**, 134502 (2017).

[18] P. K. Rout, E. Maniv, and Y. Dagan, Phys. Rev. Lett. **119**, 237002 (2017).

[19] S. Davis, Z. Huang, K. Han, T. Venkatesan, and V. Chandrasekhar, Adv. Mater. Interfaces **4**, 1600830 (2017).

[20] S. Davis, V. Chandrasekhar, Z. Huang, K. Han, Ariando, and T. Venkatesan, Phys. Rev. B **95**, 035127 (2017).

[21] N. Nakagawa, A. Y. Hwang, and A. D. Muller, Nat. Mater. **5**, 204 (2006).

[22] S. Thiel, G. Hammerl, A. Schmehl, C. Schneider, and J. Mannhart, Science **313**, 1942 (2006).

[23] M. Reinle-Schmitt, C. Cancellieri, D. Li, D. Fontaine, M. Medarde, E. Pomjakushina, C. Schneider, S. Gariglio, P. Ghosez, J.-M. Triscone, and P. Willmott, Nat. Commun. **3**, 932 (2012).

[24] N. C. Bristowe, P. B. Littlewood, and E. Artacho, Phys. Rev. B **83**, 205405 (2011).

[25] L. Yu and A. Zunger, Nat. Commun. **5**, 5118 (2014).

[26] T. C. Rödel, C. Bareille, F. Fortuna, C. Baumier, F. Bertran, P. Le Fèvre, M. Gabay, O. Hijano Cubelos, M. J. Rozenberg, T. Maroutian, P. Lecoeur, and A. S. Santander-Syro, Phys. Rev. Appl. **1**, 051002 (2014).

[27] L. Miao, R. Du, Y. Yin, and Q. Li, Appl. Phys. Lett. **109**, 261604 (2016).

[28] P. K. Rout, I. Agireen, E. Maniv, M. Goldstein, and Y. Dagan, Phys. Rev. B **95**, 241107(R) (2017).

[29] G. Drera, G. Salvinelli, A. Brinkman, M. Huijben, G. Koster, H. Hilgenkamp, G. Rijnders, D. Visentin, and L. Sangaletti, Phys. Rev. B **87**, 075435 (2013).

[30] G. Berner, A. Müller, F. Pfaff, J. Walde, C. Richter, J. Mannhart, S. Thiess, A. Gloskovskii, W. Drube, M. Sing, and R. Claessen, Phys. Rev. B **88**, 115111 (2013).

[31] See Supplemental Material at http://link.aps.org/supplemental/10.1103/PhysRevB.99.201102 for details on the theoretical modeling as well as the analysis of the Hall effect and magnetotransport data and comment on the nature of the carriers involved in multiband transport .

[32] G. Khalsa, B. Lee, and A. H. MacDonald, Phys. Rev. B **88**, 041302(R) (2013).

[33] S. Hikami, A. Larkin, and Y. Nagaoka, Prog. Theor. Phys. **63**, 707 (1980).

[34] H. Liang, L. Cheng, L. Wei, Z. Luo, G. Yu, C. Zeng, and Z. Zhang, Phys. Rev. B **92**, 075309 (2015).

[35] U. Khanna, P. K. Rout, M. Mograbi, G. Tuvia, I. Leermakers, U. Zeitler, Y. Dagan, and M. Goldstein, arXiv:1901.10931.